Power Handling of Electrostatic MEMS Evanescent-mode (EVA) Tunable Bandpass Filters

Xiaoguang Liu, *Member, IEEE,* Linda P. B. Katehi, *Fellow, IEEE,* William J. Chappell, *Member, IEEE* and Dimitrios Peroulis, *Member, IEEE*

***Abstract*—This paper presents the first theoretical and experimental study on the power handling capabilities of electrostatically-tunable MEMS cavity filters. The theoretical analysis indicates that the frequency-dependent RF voltage inside a narrow-band filter may play an important role in the generation of electromechanical non-linearities such as frequency response distortion, frequency shift and bifurcation instability. This analysis also reveals that the filter's power handling capability is dependent on several critical factors including the capacitive gap, stiffness of the diaphragm actuator, and the overall quality factor (Q) of the evanescent-mode (EVA) resonators. A non-linear CAD model is proposed as a practical tool for capturing the important trade-offs in high-power design. An EVA tunable resonator and a two-pole 2% filter are fabricated and measured as vehicles to validate the theory and the CAD model. Specifically, a medium-power filter with a tuning range of $2.35-3.21$ GHz ($1.37\ :\ 1$) and an extracted unloaded quality factor (Q_u) of $356-405$ shows measured power levels of 23.4 dBm (0.22 W) before bifurcation instability occurs. The measured IIP3 of this filter are 52.1 dBm. The theory and modeling, backed up by the measurements, provide significant insights into the high power design of electrostatic tunable cavity filters.**

***Index Terms*—non-linearity, evanescent-mode cavity filter, MEMS, quality factor (Q), tunable filter, self-actuation, inter-modulation.**

I. Introduction

Recently, MEMS evanescent-mode (EVA) tunable cavity filters for RF/microwave frequencies have received considerable research attention for their merits of wide tuning range, high unloaded quality factor (Q_u), reduced size/weight and large spurious free region [1]–[4]. Furthermore, the electrostatic MEMS tuners require almost zero DC power, making such filters great candidate components for a wide range of applications. Examples of such applications include automatic test instrumentation, wireless communication and sensing systems. These applications have varying power handling requirements, ranging from milliwatts to tens of watts. Therefore, it is important to understand the power handling capabilities of such MEMS EVA tunable filters.

The power handling capabilities of RF/microwave filters are limited by several factors including dielectric breakdown, gas discharge, thermal breakdown and device non-linearities [5]. The critical high-power phenomena for MEMS tunable filters include solid dielectric breakdown, gas discharge, and electro-mechanical non-linearities of the MEMS tuning elements. In this paper, we focus on the last one and specially in the effects of "self-actuation" and intermodulation distortion (IMD) on the power handling of MEMS EVA tunable resonators and filters. Self-actuation refers to the actuation of the movable MEMS micro-structure caused by the electrostatic attractive force stemming from the RF signal power [6]. IMD refers to the generation of unwanted amplitude modulation of signals due to device non-linearities. From a system point of view, IMD limits the maximum power a MEMS tunable filter can handle without introducing excessive in-channel and cross-channel interferences.

There have been numerous studies on the power handling of RF MEMS devices including MEMS varactors [7]–[10], capacitive switches [8], [11]–[13], and metal-contact switches [14]. In [8], theoretical analysis and CAD modeling were used to predict the power handling of MEMS varactors and switches. Girbau et al. presented extended analysis by taking into account the large displacement and impedance change during the actuation of the MEMS varactors [10]. A frequency domain analysis technique was proposed by Innocent et al. to analyze the weak non-linearities of MEMS varactors and switches [9].

However, the above mentioned modeling efforts are primarily based on stand-alone MEMS devices, such as a single MEMS varactor or switch. In [8], the non-linearities of MEMS tunable filters were studied, but the resonant characteristics of the filter were simply modeled as a voltage amplification for the MEMS devices. This is a valid approximation for filters of relatively large fractional bandwidth. However, it does not take into account the frequency dependence of the RF voltage in a resonator. In [15], the authors of this paper demonstrated the modeling and measurement of such non-linearities in high-Q_u EVA tunable cavity resonators (but not filters).

Compared to our previous work [2], [4] that focused on the design and fabrication technology of tunable EVA resonators and bandpass filters, this paper presents for the first time a complete validated framework on the power handling capability of MEMS tunable EVA filters. Building upon our previous work [15], we start by developing for the first time analytical

W. J. Chappell and D. Peroulis are with Birck Nanotechnology Center, the School of Electrical and Computer Engineering, Purdue University, West Lafayette, IN, 47906 USA e-mail: chappell@purdue.edu, and dperouli@purdue.edu.

X. Liu and L. P. B. Katehi are with the University of California, Davis, CA, USA email: liu79@purdue.edu, katehi@ucdavis.edu.

Manuscript received April 19, 2005; revised January 11, 2007.

This work has been supported by the Defense Advanced Research Projects Agency under the ASP Program with a subcontract from BAE Systems. The views, opinions, and/or findings contained in this article/presentation are those of the author/presenter and should not be interpreted as representing the official views or policies, either expressed or implied, of the Defense Advanced Research Projects Agency or the Department of Defense.

solutions for the non-linearities of MEMS EVA tunable resonators (Section II). It is shown that the frequency dependence of the RF voltage plays an important role in the modeling of the non-linearities of EVA resonators. Section III provides a practical circuit CAD model for capturing such non-linearities in a system-level environment. The theoretical and numerical models are validated in Section IV by measurements on a high-Q_u MEMS EVA tunable resonator. Power measurements on a two-pole MEMS EVA tunable filter are also presented for the first time with a very good agreement with simulation.

II. Theoretical Analysis

A. Review of MEMS EVA Tunable Cavity Resonators/Filters

Fig. 1 shows a concept drawing of the EVA tunable resonator proposed in [2]. The tunable resonator consists of an evanescent-mode resonant cavity, a thin metallic diaphragm tuner and a bias electrode placed above the diaphragm tuner. The resonant frequency and Q_u of the cavity resonator are found to be dependent on the cavity size, post size and the gap g between the post top and the top wall of the cavity. The resonant frequency is very sensitive to g when g is small. When a bias voltage is applied on the bias electrode, the thin diaphragm is pulled away from the post, changing g and thus the resonant frequency. The Q_u of this tunable resonator is inherently high due to the distributed nature of the cavity resonator. MEMS EVA tunable resonator with a tuning ratio as high as 2.6:1 and Q_u of 650 at 5 GHz has been demonstrated in [4]. The same technology was also used to make a two-pole 0.7% bandwidth filter with a tuning range of $3.0-4.7$ GHz and insertion loss of $3.55-2.88$ dB [4].

The EVA tunable resonator is a distributed implementation of a lumped element resonator [2]. The electric field is predominantly concentrated in the gap region between the capacitive post and the diaphragm, which represents an effective capacitor; the sidewalls of the cavity and the capacitive post constitute a shorted coax line, which is effectively an inductor. Therefore the EVA resonator can be modeled as an L-C tank shown in Fig. 1(c), where C_r and L_r are the equivalent capacitor and inductor respectively and R_u accounts for losses in the resonator. In the equivalent circuit of Fig. 1(c), the input and output coupling to the resonator is modeled by ideal transformers.

B. Self-actuation in MEMS EVA Tunable Resonators

MEMS EVA tunable resonators are essential building blocks of EVA tunable filters. In order to understand the power handling capability of the EVA tunable filters, it is critical to first understand the power handling capability of the EVA tunable resonators. This section focuses on the analysis of the RF self-actuation in EVA tunable resonators.

The mechanical behavior of the thin diaphragm actuator can be modeled by a simple 1-D spring-mass model shown in Fig. 1(b). The diaphragm actuator is subject to three primary forces:

1) The electrostatic force F_{DC} from the bias electrode.

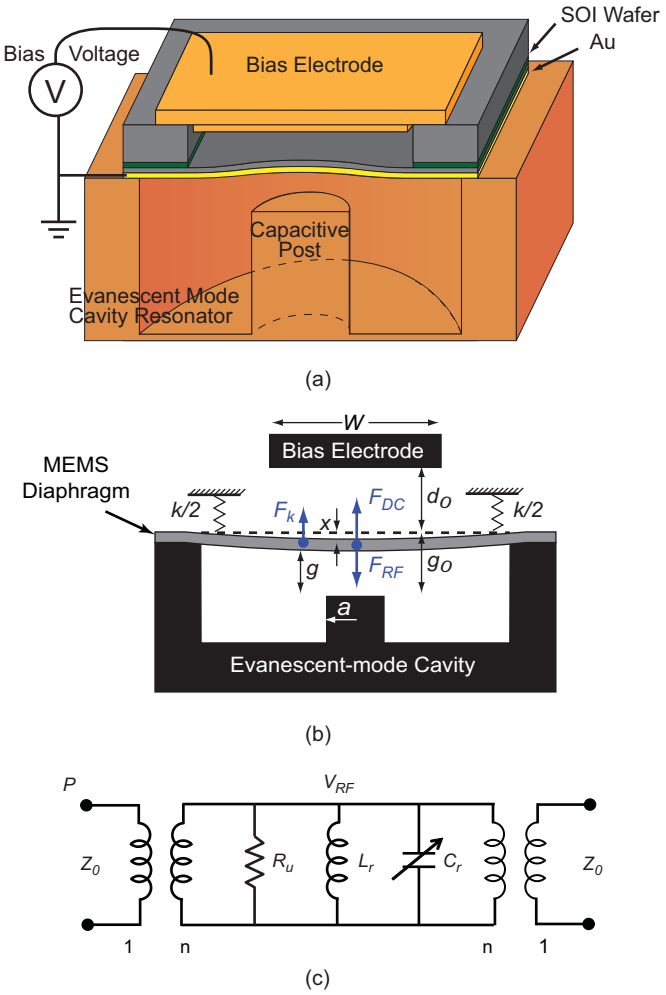

Fig. 1. (a) Concept drawing of MEMS EVA tunable resonator. (b) Spring-mass model of the MEMS diaphragm actuator. (c) Equivalent circuit of the MEMS EVA tunable resonator.

Assuming that electric field only exists in the overlapping area between the bias electrode and the diaphragm actuator, F_{DC} can be approximated by

$$F_{DC} = \frac{\epsilon_0 W^2 V_{DC}^2}{2\left(d_0 + x\right)^2}, \tag{1}$$

where W is the width of the bias electrode, V_{DC} is the bias voltage, g_0 is the initial gap between the post and the diaphragm, and x is the deflection of the diaphragm. (1) neglects the effect of the fringing-field, which can be taken into account by the non-linear circuit model explained in Section. III.

2) The electrostatic force F_{RF} from the RF signal power [6].
Using parallel-plate capacitance for C_r, F_{RF} is given by

$$F_{RF} = \frac{\epsilon_0 \pi a^2 |V_{RF}|^2}{4\left(g_0 - x\right)^2}, \tag{2}$$

where a is the post radius and V_{RF} is the peak-peak RF voltage between the post and the diaphragm. Again, the

fringing-field contribution to F_{RF} is taken into account by CAD modeling in Section. III.

3) Mechanical restoring force F_k.
Assuming linear deflection, F_k is given by

$$F_k = kx, \tag{3}$$

where k is the spring constant of the diaphragm.

In the analog tuning range mode, electro-mechanical equilibrium at a particular gao requires these forces to balance at that gap.

$$F_{DC} + F_{RF} - F_k = 0 \tag{4}$$

At low input RF power, the deflection of the diaphragm actuator is dominated by the electrostatic force between the diaphragm and the DC biasing electrode. When the input power is increased, the RF-induced electrostatic force F_{RF} starts to affect the deflection of the diaphragm. Specifically, it starts pulling the diaphragm towards the capacitive post causing non-linear responses. In a narrowband resonator/filter, this non-linear response is further pronounced by the input and output transformers.

Inserting (1), (2) and (3) into (4), we have

$$\frac{\epsilon_0 W^2 V_{DC}^2}{2\left(d_0+x\right)^2} - \frac{\epsilon_0 \pi a^2 |V_{RF}|^2}{4\left(g_0-x\right)^2} + kx = 0 \tag{5}$$

Note that the DC bias increases the capacitive gap g and therefore reduces F_{RF}. In other words, when a DC bias is applied to tune the resonant frequency higher, the power handling capability will also increase. Therefore, the worst case scenario is seen when no DC bias is applied. In the following analysis we assume no DC bias and look at the non-linear response of the EVA tunable resonators solely due to RF power. As will be shown later, omitting the DC bias signal effect does not undermine the generality of the conclusions drawn from the analysis presented in this section.

With no DC electrostatic force, (5) is simplified as

$$\epsilon_0 \pi a^2 |V_{RF}|^2 = 4kx(g_0-x)^2, \tag{6}$$

V_{RF} can be calculated by linear circuit analysis of Fig. 1:

$$V_{RF} = \frac{2}{\left(j\omega C_r + \dfrac{1}{j\omega L_r} + \dfrac{1}{R_u}\right) + \dfrac{2}{n^2 Z_0}} \sqrt{\frac{2P}{n^2 Z_0}}, \tag{7}$$

where n is the transformation ratio, Z_0 is the port impedance and P is the RF power from the input port.

Inserting (7) into (6) and rearranging both sides of the equation, we get

$$\frac{2\epsilon_0 \pi a^2 P}{n^2 Z_0} = kx(g_0-x)^2 \left| \left(j\omega C_r + \frac{1}{j\omega L_r} + \frac{1}{R_u}\right) + \frac{2}{n^2 Z_0} \right|^2 \tag{8}$$

Note that C_r is directly related to the deflection of the MEMS actuator. We use the parallel-plate model for the capacitance calculation. The neglected fringing-field term is taken into account in the circuit models developed in Section. III.

$$C_r = \frac{\epsilon \pi a^2}{g_0 - x} \tag{9}$$

Putting (9) into (8) and rearranging both sides, we get

$$\frac{2\epsilon_0 \pi a^2 P(\omega L_r)^2}{n^2 Z_0} = kx \Bigg\{ \left[\epsilon_0 \pi a^2 \omega^2 L_r - (g_0 - x)\right]^2 + (g_0-x)^2(\omega L_r)^2 \left(\frac{1}{R_u} + \frac{2}{n^2 Z_0}\right)^2 \Bigg\}. \tag{10}$$

Eq. (10) can be further simplified by making a few more substitutions

$$\frac{x}{g_0} \left\{ \left[\left(\frac{\omega}{\omega_0}\right)^2 - \frac{g_0 - x}{g_0} \right]^2 + \left(\frac{g_0 - x}{g_0}\right)^2 \left(\frac{\omega}{\omega_0}\right)^2 / Q^2 \right\} = \left(\frac{\omega}{\omega_0}\right)^2 F, \tag{11}$$

where

$$\omega_0^2 = \frac{1}{L_r C_c} = \frac{g_0}{\epsilon_0 \pi a^2 L_r},$$

is the small-signal resonant frequency of the resonator,

$$Q = \frac{1}{\omega_0 L_r \left(\dfrac{1}{R_u} + \dfrac{2}{n^2 Z_0}\right)},$$

is the doubly loaded quality factor of the resonator and

$$F = \frac{2\epsilon_0 \pi a^2 P \omega_0^2 L_r^2}{k n^2 Z_0 g_0^3} = \frac{2PL_r}{k n^2 Z_0 g_0^2}.$$

We now define a normalized varactor gap

$$\hat{g} = \frac{g_0 - x}{g_0},$$

and normalized frequency

$$\hat{\omega} = \left(\frac{\omega}{\omega_0}\right)^2.$$

(11) can then be further simplified

$$(1-\hat{g}) \left[(\hat{\omega} - \hat{g})^2 + \frac{\hat{g}^2 \hat{\omega}}{Q^2} \right] = \hat{\omega} F, \tag{12}$$

Eq. (12) is the non-linear equation describing the relationship between the normalized deflection of the diaphragm and the RF power. It is a 3rd order equation in terms of $\hat{g}$ and has three solutions in the complex domain. Among the three solutions, the ones in the real domain give the amplitude of the normalized diaphragm deflection under certain external RF power.

For small input power, i.e. small F, only one solution is in the real domain. This corresponds to the case of small signal

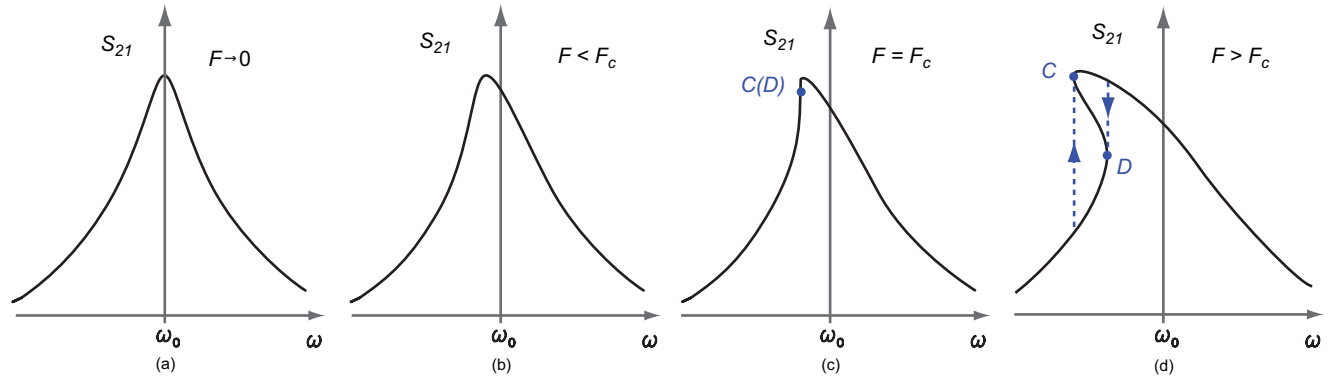

Fig. 2. Frequency responses of the non-linear MEMS EVA resonator with different input power levels. (a) Symmetric response with very small input; (b) Frequency distortion with medium input power; (c) Onset of bifurcation; (d) Bifurcation.

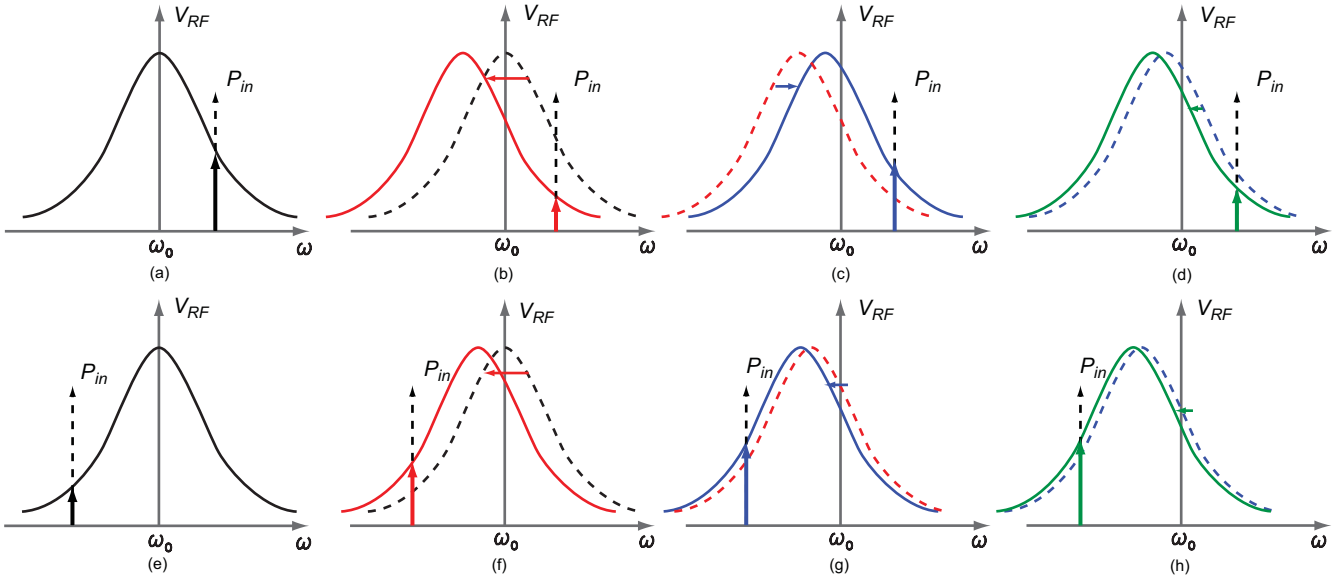

Fig. 3. Conceptual explanation of the frequency distortion with moderate input power. (a-d) Input signal higher than the resonant frequency leads to a negative feedback process; (e-h) Input signal lower than the resonant frequency leads to a positive feedback process.

input (Fig. 2 (a)). In the limiting case of $F \to 0$, the frequency response of the resonator is symmetrical around the resonant frequency.

As F increases, the resonant frequency becomes lower and the frequency response starts to "bend" towards it. This asymmetrical distortion in the frequency response can be intuitively understood if we consider the establishment of the frequency response in an iterative manner.

Fig. 3(a-d) shows the case when a moderately high power input RF signal is applied at a frequency higher than the resonant frequency. F_{RF} pulls the diaphragm actuator closer to the capacitive post, thus lowering the resonant frequency. This in turn lowers V_{RF} and F_{RF}, causing a negative feedback effect. Due to the mechanical restoring force, the diaphragm actuator will retract away from the post until an equilibrium is achieved.

When the input signal is applied at a lower frequency, as shown in Fig. 3(e-h), the scenario can be quite different. The V_{RF} lowers the resonant frequency in a similar fashion as in the previous case. However, as the resonant frequency moves closer to the input signal, the induced V_{RF} increases, creating a positive feedback process. Due to this increased V_{RF}, the resonant frequency will become still lower until equilibrium is achieved.

From this conceptual experiment, it is obvious that the EVA resonator reacts differently to input RF signals below and above its resonant frequency. This behavior leads to the asymmetrical response shown in Fig. 2. It is worth noting that the frequency response curves in Fig. 3 are all drawn in linear scale for easier illustration.

When the input power becomes even larger, the situation becomes more complex as F reaches a critical value F_c. It is noted that there is still a one-to-one correspondence between $\hat{g}$ and $\hat{\omega}$ for $F < F_c$. For $F > F_c$, however, all 3 solutions to (12) can be real. In this case, there are three possible $\hat{g}$ values for a certain range of frequencies $\hat{\omega}_1 < \hat{\omega} < \hat{\omega}_2$ (Fig. 2 (d)). Such a phenomena is often referred to as "*bifurcation*" [20].

C. Critical RF Power

In order to predict the critical power handling capability of MEMS EVA tunable resonators and filters, it is important to calculate the value of the critical input RF power P_c, which presents itself in (12) as F_c. We first observe that the condition $d\hat{g}/d\hat{\omega} = \infty$ holds at $\hat{\omega}_1$ and $\hat{\omega}_2$ (which correspond to points C and D in Fig. 2(d)). Differentiating (12) with respect to $\hat{\omega}$, yields

$$(1-\hat{g})\left[2(\hat{\omega}-\hat{g})\left(1-\frac{d\hat{g}}{d\hat{\omega}}\right)+\frac{2\hat{g}\hat{\omega}}{Q^2}\frac{d\hat{g}}{d\hat{\omega}}+\frac{\hat{g}^2\hat{\omega}}{Q^2}\right]- \frac{d\hat{g}}{d\hat{\omega}}\left[(\hat{\omega}-\hat{g})^2+\frac{\hat{g}^2\hat{\omega}}{Q^2}\right]=F \tag{13}$$

In order to satisfy the condition $d\hat{g}/d\hat{\omega} = \infty$, we set the coefficient of the $d\hat{g}/d\hat{\omega}$ term in (13) to zero.

$$2(1-\hat{g})\frac{\hat{g}\hat{\omega}}{Q^2}-2(1-\hat{g})(\hat{\omega}-\hat{g})-(\hat{\omega}-\hat{g})^2-\frac{\hat{g}^2\hat{\omega}}{Q^2}=0,$$

which can be rearranged as a quadratic equation in terms of $\hat{\omega}$

$$\hat{\omega}^2-\left(\frac{2\hat{g}}{Q^2}-\frac{3\hat{g}^2}{Q^2}+4\hat{g}-2\right)\hat{\omega}+(3\hat{g}^2-2\hat{g})=0. \tag{14}$$

$\hat{\omega}_1$ and $\hat{\omega}_2$ can then be found by simultaneously solving (14) and (12).

However, the calculation of F_c does not require the solution for $\hat{\omega}_1$ and $\hat{\omega}_2$. We observe that points C and D reduce to a single point when $F = F_c$ (Fig. 2(c)). In other words, the two solutions to (14) coincide with each other. Setting the discriminant of (14) to zero, we get

$$\left(\frac{2\hat{g}}{Q^2}-\frac{3\hat{g}^2}{Q^2}+4\hat{g}-2\right)^2-4(3\hat{g}^2-2\hat{g})=0 \tag{15}$$

Eq. (15) is a 4th order equation in terms of $\hat{g}$ and has four solutions in the complex domain. Of the four solutions, only one is physically meaningful ($0 < \hat{g} < 1$). It gives the normalized gap value $\hat{g}_c$ that corresponds to point $C(D)$ in Fig. 2(c). Its close-form formula is rather involved but can be analytically found by using the root-finding formula or more conveniently, a symbolic mathematics software package such as *Mathematica* [19].

With the help of *Mathematica*, we can use the power series expansion to get a more practical and simplified formula for $\hat{g}_c$. In the limit of $Q \gg 1$,

$$\hat{g}_c = 1-\frac{1}{Q}+\frac{3}{Q^2}-O(Q^3) \tag{16}$$

Putting (16) into (14), we can find the normalized frequency $\hat{\omega}_c$ at which bifurcation occurs,

$$\hat{\omega}_c = 1-\frac{2}{Q}+\frac{11}{2Q^2}-O(Q^3) \tag{17}$$

Putting (16) and (17) into (12), we can solve for F_c

$$F_c = \frac{2}{Q^2}+\frac{11}{Q^3}-O(\frac{1}{Q^4}) \tag{18}$$

Therefore

$$P_c = \frac{kZ_0g_0^2}{2L}\left[\frac{2}{Q^2}+\frac{11}{Q^3}-O(\frac{1}{Q^4})\right] \tag{19}$$

At the onset of bifurcation, the critical deflection x_c and frequency f_c are respectively

$$x_c = g_0\left[\frac{1}{Q}-\frac{3}{Q^2}+O(Q^3)\right] \tag{20}$$

$$f_c = \frac{\omega_0}{2\pi}\left[1-\frac{2}{Q}+\frac{9}{4Q^2}-O(Q^3)\right] \tag{21}$$

It is also interesting to note that in the limit of $Q \to 0$, the solution to (14) can be expanded (using *Mathematica*) as

$$\hat{g}_c = \frac{2}{3}-\frac{1}{3}Q^2+\sqrt{\frac{2}{3}}Q^3-O(Q^4) \tag{22}$$

and

$$\hat{\omega}_c = \sqrt{\frac{2}{3}}Q-Q^2-\sqrt{\frac{2}{3}}Q^3+O(Q^4) \tag{23}$$

This is intuitively understood because as $Q \to 0$, the resonator is heavily loaded and approaches a transmission structure instead of a resonant structure. The bifurcation instability occurs at DC ($\hat{\omega}_c \to 0$) at an normalized gap of $\hat{g}_c \to \frac{2}{3}$, which is simply the instability point of an electrostatically actuated parallel plate actuator [6]. Therefore, the DC instability can be regarded as a special case of the analysis developed in this section.

Eq. (19) gives the critical input power level at the onset of bifurcation. Note that DC bias is assumed to be zero in the above analysis. Therefore (19) gives the minimum upper limit of power handling capability of an MEMS EVA tunable resonator.

P_c in (19) is shown to be dependent on a few factors, including the stiffness k of the diaphragm actuator, initial gap g_0, and the overall quality factor Q. Whereas Q is often determined by system level requirements, appropriate k and g_0 can be chosen to improve the power handling capabilities of MEMS EVA tunable resonators/filters. However, in most applications, other specifications, such as actuation voltage and tuning, often need to be taken into account as well. For example, improving power handling capability by increasing k and g_0 comes at the cost of increased actuation voltage or reduced tuning range. These inter-dependencies are examined quantitatively in Section III.

It is important to mention that the analysis given in this section is based on a general non-linear varactor model and the general conclusions from the above analysis hold true for any tunable resonator using parallel plate electrostatic MEMS switches/varactors as the tuning elements.

D. MEMS EVA Tunable Filters

The self-actuation behavior of MEMS EVA tunable filter can be analyzed following a similar approach as the EVA tunable resonator. Fig. 4 shows a schematic of a general coupled-resonator bandpass filter. $M_{i,j}$ are the elements of the coupling matrix and denote the direct- and cross- coupling between the resonators [17].

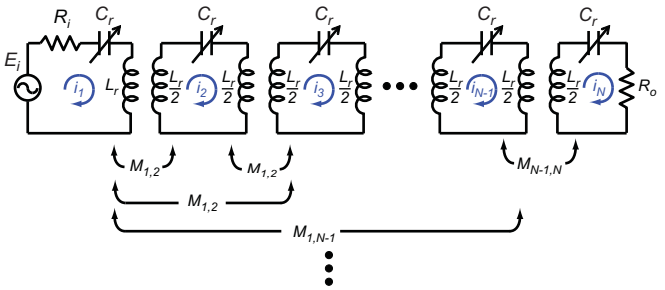

Fig. 4. Schematic of a general coupled-resonator MEMS EVA tunable filter. The graph follows the convention of [17].

The loop equations for each of the resonators in the filter can be written in a matrix form (Eq. 24).

With knowledge of the coupling matrix, the current in each resonator can be solved. The voltage on the j^{th} MEMS varactor is then given by

$$V_{RF_j} = \frac{i_j}{j\omega C_r} \tag{25}$$

Inserting (25) and (9) into (5), one can obtain the non-linear equation describing the self-actuation behavior of the EVA tunable filters. However, this equation can become very complicated for higher order filters. A simpler and more practical way of solving the non-linear equation is through the use of a numerical CAD model, which is the subject of the following section.

III. CAD Modeling

In the previous section, theoretical analysis on non-linearity of the MEMS EVA tunable resonator is presented. It is important to develop a more practical design tool in order to take into account second-order effects such as fringing field capacitance and model more complicated structures such as higher order filters. This section presents the modeling of non-linearities of EVA tunable resonators through a nonlinear CAD model.

A. Non-linear CAD Model

The analysis of Section II-B shows that the non-linearity of the EVA tunable resonator is primarily caused by the non-linearity of the equivalent varactor C_r. The electro-mechanical characteristics of C_r are governed by V_{DC} (Eq. 1), V_{RF} (Eq. 2) and F_k (Eq. 3). These equations are coupled with each other and analytical solutions are difficult to obtain. However, an iterative approach can be utilized to numerically solve these equations.

Fig. 5 outlines this process. First the RF voltage V_{RF} across the varactor C_r is found from (7) by setting C_r to its initial value, i.e. the mechanical deflection of the diaphragm is only determined by the DC bias voltage V_{DC}. Then V_{RF} is used to calculate the RF force F_{RF} exerted on the diaphragm according to (2). F_{RF} is in turn used to calculate the deflection x of the diaphragm, which gives an updated value to C_r. This process is repeated until the solution converges. A failed convergence indicates that the RF power is large enough to cause self-pullin of the diaphragm.

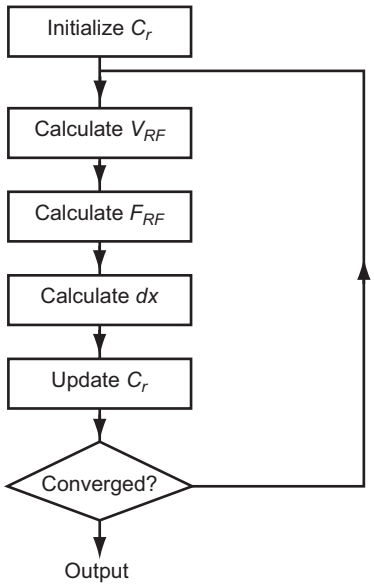

Fig. 5. Procedure for iteratively solving the coupled non-linear equations (1),(2),(3),(4) and (7).

The above process can also be implemented using commercially-available circuit simulators. Building upon previous work by Lu [18], a non-linear voltage controlled capacitor model (Fig. 6) is constructed in Agilent Advanced Design Systems (ADS) using 4-port Symbolically-Defined Devices (SDD) [21].

The voltages at the four ports of the model are defined as follows:

1) Port 1: Diaphragm deflection x;
2) Port 2: Electrostatic force on the diaphragm $F_e = F_{RF} + F_{DC}$;
3) Port 3: RF voltage V_{RF};
4) Port 4: DC bias voltage V_{DC}.

An example EVA tunable resonator is simulated with the equivalent non-linear circuit model. The resonant frequency and Q_u of the resonator are 2.4 GHz and 1000 respectively. The external quality factor Q_e is assumed to be 50. The nominal parameters of the tunable resonator are listed in Table I. Fig. 7 shows the simulated large-signal S_{21} at different input power levels with no DC biasing.

The simulation shows that for the particular design parameters and for low input power signals (< 10 dBm), S_{21} remains quite linear. As the input power is increased, non-linearities start to appear. For input power in the range of $15 \sim 20$ dBm, self-biasing causes the diaphragm to deflect towards the capacitive post, leading to a drift in the resonant frequency and distortion to the shape of the resonance peak.

$$\begin{bmatrix} E_i \\ 0 \\ 0 \\ \cdot \\ \cdot \\ \cdot \\ 0 \\ 0 \end{bmatrix} = \begin{bmatrix} j\omega L_r + \frac{1}{j\omega C_r} + R_i & jM_{1,2} & jM_{1,3} & \cdot & \cdot & \cdot & jM_{1,N} \\ jM_{1,2} & j\omega L_r + \frac{1}{j\omega C_r} & jM_{2,3} & \cdot & \cdot & \cdot & \cdot \\ jM_{1,3} & jM_{2,3} & j\omega L_r + \frac{1}{j\omega C_r} & \cdot & \cdot & \cdot & \cdot \\ \cdot & \cdot & \cdot & \cdot & \cdot & \cdot & \cdot \\ \cdot & \cdot & \cdot & \cdot & \cdot & \cdot & \cdot \\ \cdot & \cdot & \cdot & \cdot & \cdot & \cdot & \cdot \\ jM_{1,N-1} & \cdot & \cdot & \cdot & \cdot & j\omega L_r + \frac{1}{j\omega C_r} & jM_{N-1,N} \\ jM_{1,N} & \cdot & \cdot & \cdot & \cdot & jM_{N-1,N} & j\omega L_r + \frac{1}{j\omega C_r} + R_o \end{bmatrix} \times \begin{bmatrix} i_1 \\ i_2 \\ i_3 \\ \cdot \\ \cdot \\ \cdot \\ i_{N-1} \\ i_N \end{bmatrix} \tag{24}$$

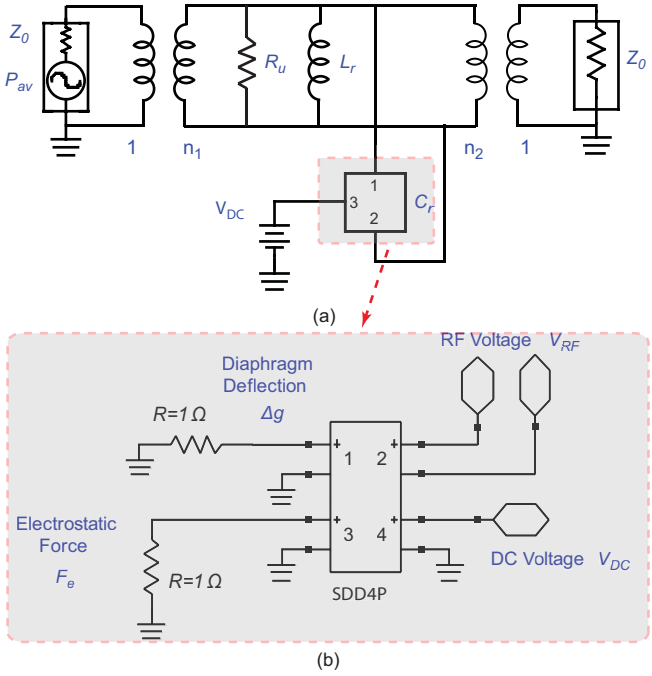

Fig. 6. (a) Non-linear circuit model for the EVA tunable resonator. (b) Non-linear varactor model using Agilent Advanced Design Systems (ADS) 4-port Symbolically-Defined Devices (SDD).

TABLE I
NOMINAL PARAMETERS OF THE SIMULATED EVA TUNABLE RESONATOR

r	Capacitive Post Radius	0.5 mm
A	Bias Electrode Size	6×6 mm^2
W	Diaphragm Side Width	7 mm
g_0	Initial Capacitive Gap	5 μm
d_0	Initial Actuation Gap	40 μm
Q_u	Unloaded Quality Factor	1000
Q_e	External Quality Factor	50
L_r	Equivalent Inductance	3.16 nH
R_u	Equivalent Shunt Resistance	47627 Ω
k	Spring Constant	400 N/m
Q_m	Mechanical Quality Factor	0.2

At a power of $\sim$ 30 dBm, the RF induced attractive force is sufficiently large to pull the diaphragm into the capacitive post. This can be seen in the instability point of the diaphragm deflection plot in Fig. 7, where a sudden jump in the diaphragm deflection is observed. When the diaphragm is pulled into the post, the resonator cannot be tuned any more. The diaphragm will restore to its original position when the RF power is turned off. Assuming no dielectric discharge or breakdown, the critical power P_c sets the higher limit to the power handling capabilities of the MEMS EVA tunable resonators.

B. High Power Design Considerations

It is shown in (19) that the critical power P_c is strongly dependent on the overall quality factor Q. Q is related to the unloaded quality factor Q_u and external quality factor Q_e by

$$\frac{1}{Q} = \frac{1}{Q_u} + \frac{1}{Q_e}. \tag{26}$$

Whereas Q_u is often determined by the resonator technology, Q_e can vary considerably according to the design's specifications. Fig. 8 shows the calculated large-signal S_{21} at the onset of instability for resonators with different Q_e. Linear responses are included as a comparison. The nominal parameters of the resonators in this calculation are listed in Table I.

It is shown in (19) that the power handling capability is also dependent on the gap g and spring constant k. Fig. 9(a) shows the large signal S_{21} for resonators with the same input power of 33.8 dBm but varying g_0 of 2 μm, 5 μm, 10 μm, and 20 μm. The nominal parameters of the resonators are shown in Table I. The resonant frequencies are kept the same for all resonators by setting the post radii values to 0.316 mm, 0.5 mm, 0.707 mm, 1 mm respectively. With 33.8 dBm input power, the frequency response of the resonator with $g_0 =$ 10 μm is at the onset of bifurcation. For smaller g_0 (5 μm and 10 μm), severe bifurcation can be observed; for larger g_0 (20 μm), the frequency response is much less distorted. Similarly, Fig. 9(b) shows the large signal S_{21} for resonators with varying spring constant. It is seen that the power handling is improved with increasing spring constant.

The penalties paid with increasing g_0 and k are reduced tuning range or higher actuation voltage. For example, Fig. 10 shows the calculated actuation voltage of a tunable resonator (parameters listed in Table I) with respect to k and g_0 for $1.5:1$ tuning ratio. It can be seen that P_c can be increased by 20 dBm by increasing g_0 from 2μm to 10μm. The required actuation voltage needs to be increased by almost 400 V to maintain the same tuning ratio.

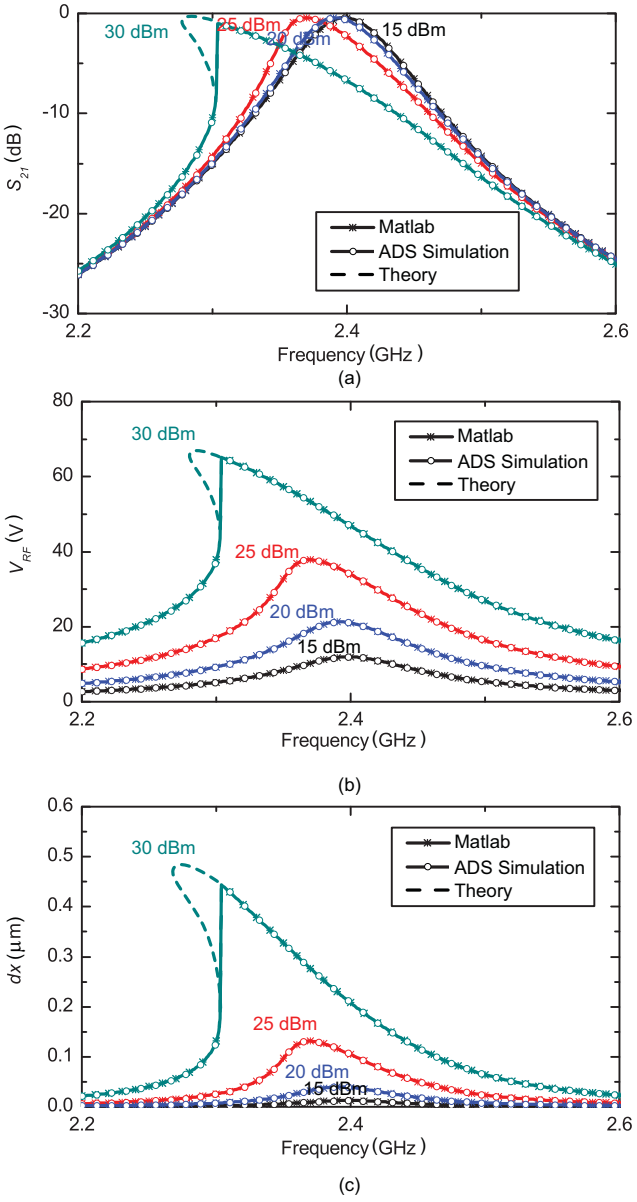

Fig. 7. ADS simulation of large signal responses of a MEMS EVA tunable resonator using non-linear circuit model shown in Fig. 1. (a) S_{21}; (b) RF voltage on the varactor; (c) Diaphragm deflection under different input power levels.

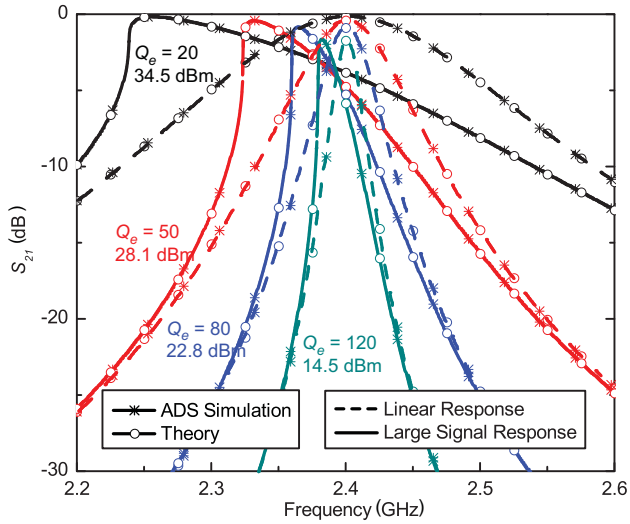

Fig. 8. Large-signal simulation of resonators with different external couplings.

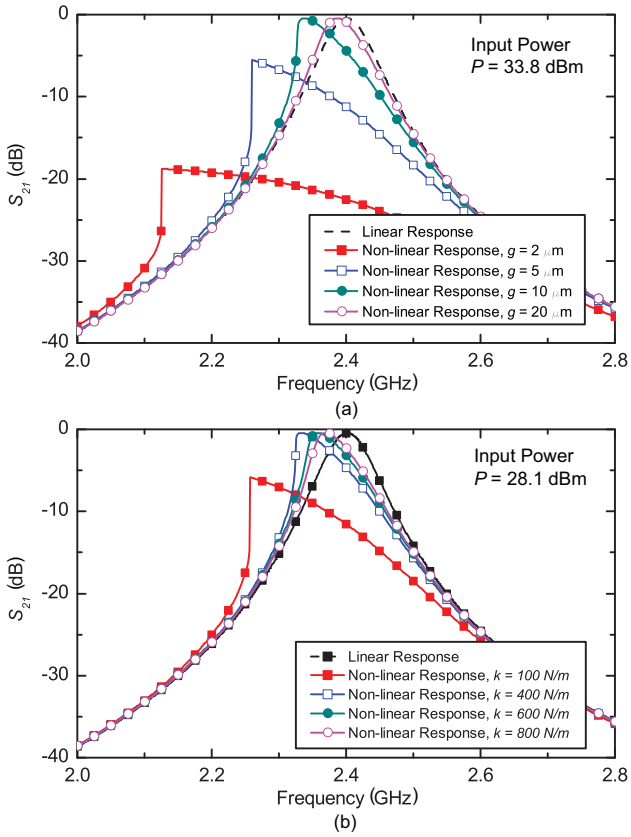

Fig. 9. Large signal simulation of resonators with (a) different capacitive gaps, and (b) different spring constant. The resonant frequency and C_r are kept the same by setting appropriate post radius. The nominal parameters of the simulated resonator is listed in Table I.

C. DC Bias

Section III-B shows that high RF signal power can lead to a shift in the resonant frequency. This shift is always towards the lower frequency due to the attractive electrostatic force. Intuitively, this frequency shift can be compensated by increasing the DC bias voltage, which serves to pull the diaphragm actuator away from the post and increase the resonant frequency.

Fig. 11 shows the simulated linear and non-linear response of a tunable resonator with 26 dBm input power. The nominal parameters of the resonator are listed in Table I. The dashed curve represents the linear response of the resonator with no DC bias voltage. The dotted curves represents the non-linear frequency response when an input RF power of 26 dBm is fed through the resonator. A close-up plot of the frequency response at 2.4 GHz is shown in Fig. 11(b). With 26 dBm input power and no DC bias, a frequency shift of 40 MHz can be observed. The solid curve shows that this frequency shift can be compensated by applying 25 V bias voltage. However, the asymmetric distortion can still be observed in the frequency response. Although additional DC biasing can compensate for

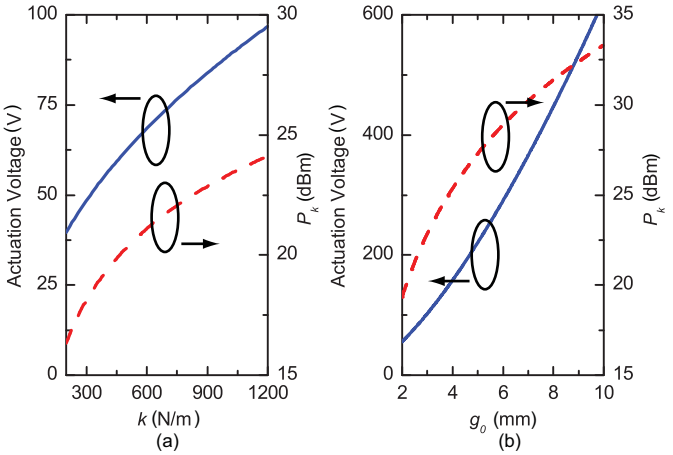

Fig. 10. Simulated actuation voltage and P_c of the EVA tunable resonator with respect to (a) the spring constant and (b) the initial gap. The nominal parameters of the simulated resonator are listed in Table I.

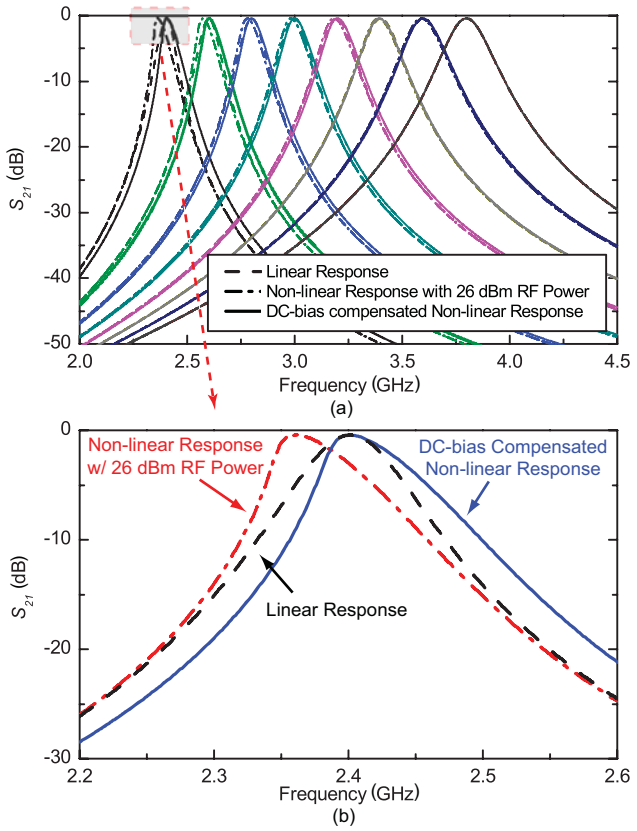

Fig. 11. (a) Simulated linear and non-linear responses of an EVA tunable resonator with varying DC bias voltages. (b) Close-up plot of the tunable resonator at 2.4 GHz showing compensation for frequency drift by applying additional DC bias.

the frequency shift, it cannot prevent the self-pullin instability in EVA tunable resonators.

Fig. 11 also shows that the frequency distortion is less severe at higher frequencies. This is primarily due to the fact that the diaphragm actuator is farther away from the post and P_c increases proportional to g_0^2 as shown in (19).

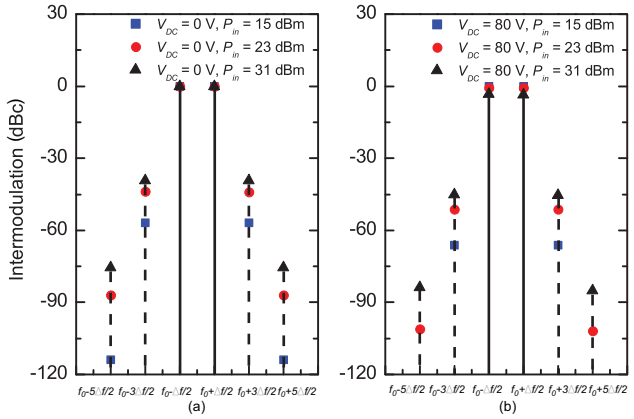

Fig. 12. Simulated spectrum of IMD products of an EVA tunable resonator with (a) 0 V and (b) 80 V actuation voltage. Parameters of the simulated resonator is listed in Table I

D. Intermodulation

With the non-linear model developed in previous sections, the intermodulation distortion of EVA tunable resonators can be quantitatively investigated.

Fig. 12 shows simulated intermodulation products of an EVA tunable resonator in response to two-tone input signals. The nominal parameters of the resonator are listed in Table I. The frequency separation of the two-tone input signals is 10 kHz, which is the mechanical resonant frequency of the diaphragm actuator. The 3rd order intermodulation product (IM3) of the tunable resonator with 0 V and 80 V bias are compared in the plot (the resonant frequencies are 2.4 GHz and 2.8 GHz respectively). Slightly smaller IM3 is observed for the 80 V case due to the higher capacitive gap g.

Fig. 13 shows the comparison of the output powers of the fundamental frequency and the IM3 products. With small input power (< 20 dBm), both the fundamental output and the IM3 increases linearly with the input power. As the input power increases, compression of both the fundamental output and the IM3 can be observed. This compression is caused by the self-actuation of the diaphragm actuator, leading to a lowering in resonant frequency and thus an increase in return loss for the input signals.

E. Non-linearities of EVA Tunable Filters

With the non-linear CAD resonator model, the high-power response of coupled-resonator EVA filters can also be quantitatively investigated. Fig. 14 shows the simulated responses of a two-pole and a four-pole direct-coupled Butterworth filter at 2.4 GHz with 2% fractional bandwidth. The filters are designed with 2 and 4 resonators respectively. The nominal parameters of the resonators are the same as those listed in Table I. The inter-resonator couplings are achieved with J-inverters, which are modeled by T-section inductor networks.

The RF voltages are different on each resonator in a coupled-resonator filter. Therefore the power handling is determined by the resonator that experiences the highest RF voltage. The RF voltage distribution is in general dependent on the internal and external coupling coefficients of the filter.

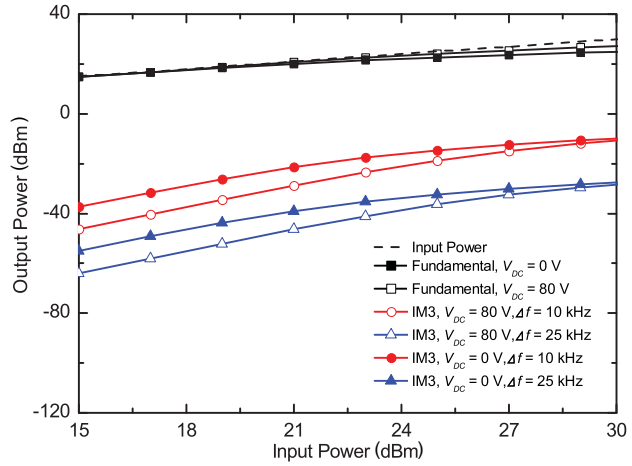

Fig. 13. Simulated output power of an EVA tunable resonator with respect to input power. Parameters of the simulated resonator is listed in Table I

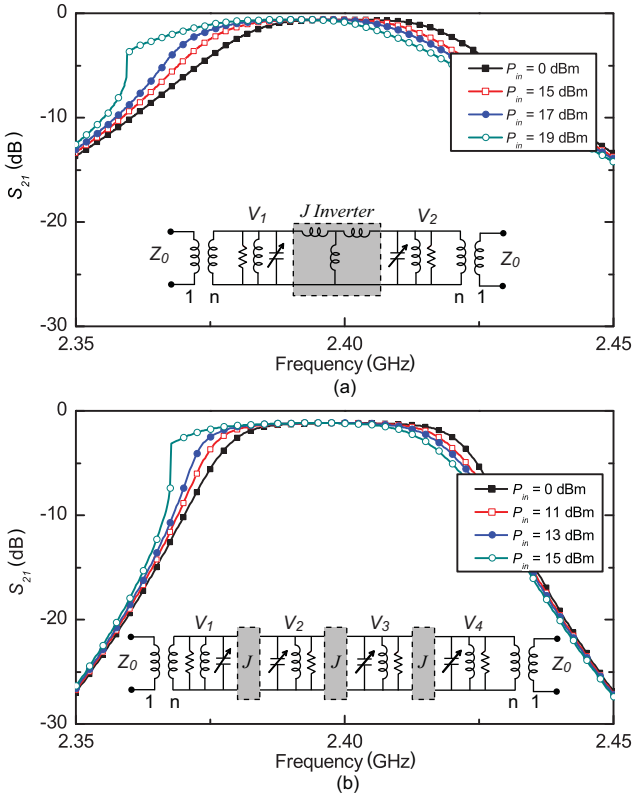

Fig. 14. Simulated non-linear responses of (a) two-pole and (b) four-pole 2% Butterworth filter.

Fig. 15 shows the simulated RF voltages on the resonators in the two-pole and four-pole filters with identical input and output couplings. In general, the second resonator sees the highest voltage at the band edge. In the two-pole filter case the first resonator sees the highest voltage. The power handling capability of the filter is determined by the P_c of this resonator. The non-linear model can also be used when the input and output coupling coefficients are not identical.

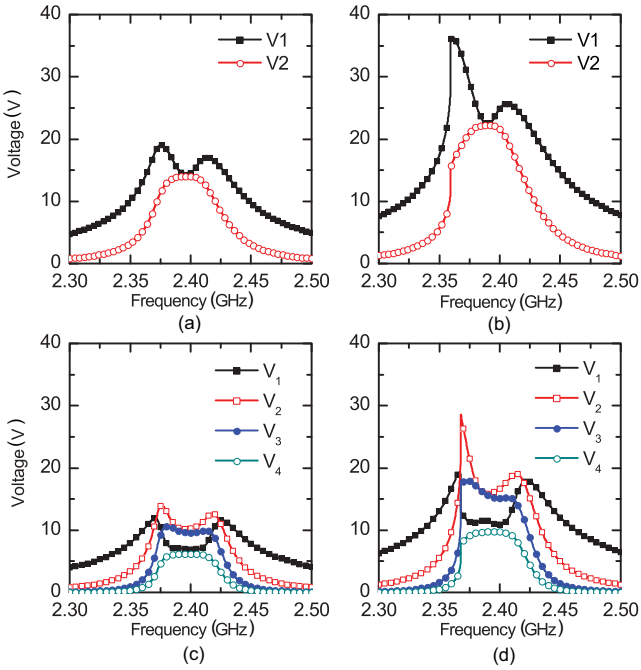

Fig. 15. Simulated RF voltage on the resonator in a two-pole filter and four-pole filter. (a)$P_{in} = 15$ dBm; (b)$P_{in} = 19$ dBm; (c) $P_{in} = 11$ dBm; (d) $P_{in} = 15$ dBm.

IV. Experimental Validation

A. MEMS EVA Tunable Resonator

A MEMS EVA tunable resonator has been fabricated and measured to validate the theoretical and numerical models developed in the previous sections. The design procedure and fabrication techniques are presented in [2]. Fig. 16(a) shows the CAD drawing of the EVA tunable resonator. Fig. 16(b,c) shows the fabricated EVA cavity and assembled EVA tunable resonator.

Small signal S-parameter measurements were taken using an Agilent 8722ES vector network analyzer (VNA). The CPW feedlines of the resonator are shorted by two pieces of copper tapes to achieve weak coupling so that the Q_u of the resonator can be extracted with higher accuracy. In large signal measurements, the copper tapes can be removed to achieve stronger coupling (Fig. 16).

The measured resonator has a tuning range of $1.85 - 2.84$ GHz $(1.51 : 1)$ with less than 140 V actuation voltage. The high actuation voltage required for achieving this tuning range can be supplied by a voltage driver [22], [23]. The critical parameters of the EVA tunable resonator, such as Q_u, g_0 and etc, are extracted from the small signal measurements. The overall Q of the resonator is related to Q_u and Q_e by (26). In a weakly-coupled resonator, the Q_e is sufficiently large so that the $1/Q_e$ term can be neglected and the measured Q approaches Q_u. The capacitive gap g is extracted by matching the HFSS model of the resonator to the measured initial resonant frequency [2]. The initial gap of the resonator is 9 μm and the diaphragm deflects 14 μm before pullin. The actuation gap d_0 is approximated to be three times the maximum deflection. The spring constant of the diaphragm

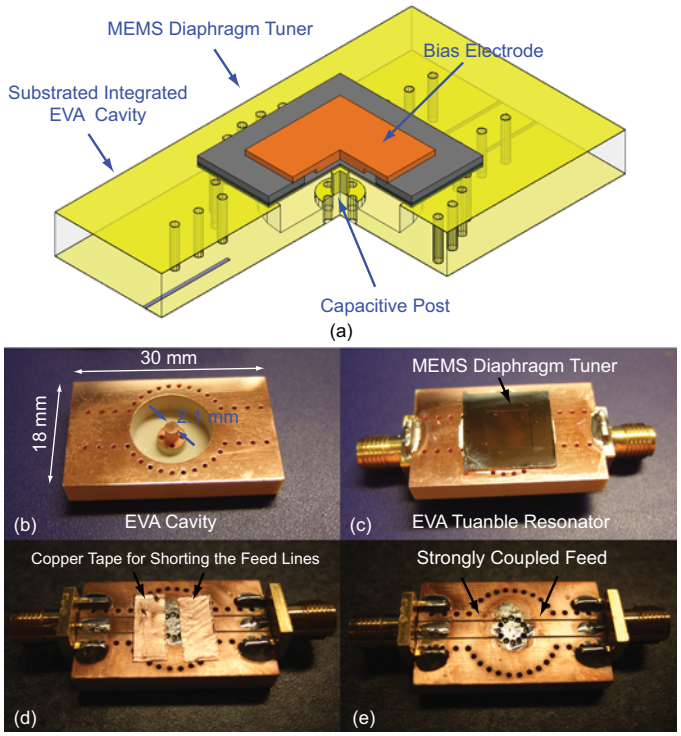

Fig. 16. (a) Illustration of the EVA tunable resonator design. (b) The fabricated EVA cavity. (c) EVA tunable resonator. (d) Copper tapes are used to short the feed lines to achieve weak coupling. (e) CPW feed on the backside of the resonator for strong coupling. The bias electrode is not shown in the picture to reveal the Si/Au diaphragm actuator.

actuator is calculated by the pullin voltage equation (Eq. 27).

$$V_{pi} = \sqrt{\frac{8kd_0^3}{27\epsilon_0 W^2}} \tag{27}$$

TABLE II
EXTRACTED PARAMETERS OF THE MEASURED EVA TUNABLE RESONATORS

r	Capacitive Post Radius	1.05 mm
A	Bias Electrode Size	6×6 mm^2
W	Diaphragm Side Width	7 mm
g_0	Initial Capacitive Gap	9 μm
d_0	Initial Actuation Gap	42 μm
k	Spring Constant	450 N/m
Q_u	Unloaded Quality Factor	270 @ 2 GHz
Q_e	External Quality Factor	43
L_r	Equivalent Inductance	1.62 nH
Q_m	Mechanical Quality Factor	0.2

Fig. 17 shows the high power measurement setup used to characterize the self-actuation of the EVA tunable resonator. A 43 dB gain power amplifier (Mini-Circuits ZHL-16W-42+) is used to amplify the frequency sweep signal from the VNA. The output of the amplifier is protected by a circulator with its isolation port terminated with a 50 Ω load. The amplified signal goes through the EVA resonator and is attenuated by a 20 dB attenuator before going back to the VNA. The setup is calibrated with Agilent 85052D 3.5 mm kit to the end of the input and output port cables of the VNA. The insertion

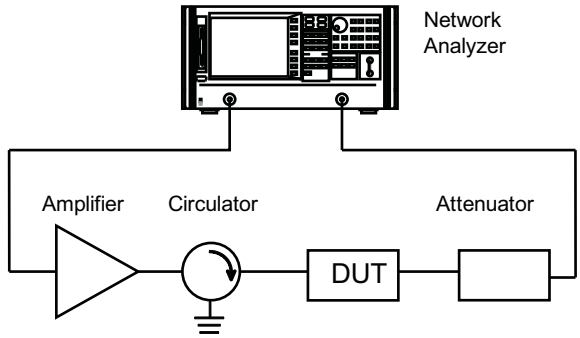

Fig. 17. Measurement setup for self-actuation characterization.

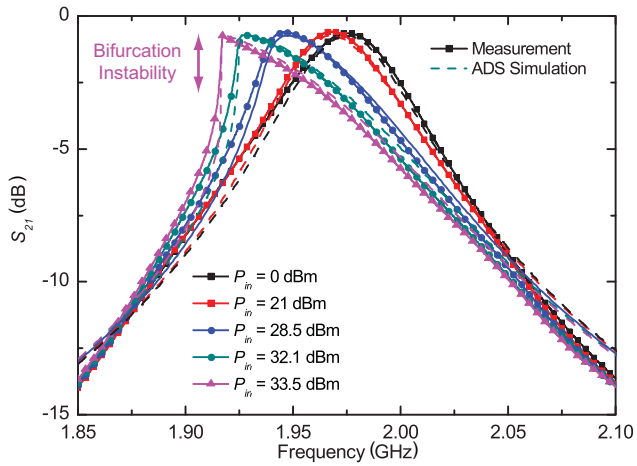

Fig. 18. The measured and simulated self-actuation characteristics of the EVA tunable resonator.

loss of the circulator and the attenuator are subtracted from the measured S_{21}.

The measured large-signal frequency responses with several input power levels are shown in Fig. 18. With the current setup, reflection coefficients of the filter can not be measured and therefore are not presented here. With low RF power ($<$ 21 dBm), there is little distortion to the frequency response. As the RF power increases (21 dBm and 28.5 dBm), the S_{21} exhibits distortion as predicted by the theory and CAD modeling. The onset of instability occurs at 32.1 dBm (1.62 W). As the input power is further increased to 33.5 dBm, a discontinuity in S_{21} can be observed. The measured results agree very well with ADS simulations. The parameters used in the simulation are listed in Table II.

The intermodulation behavior of the EVA tunable resonators is measured by the 2-tone setup shown in Fig. 19. Two Agilent 4433B signal generators were used to generate the 2-tone signals, which are then amplified and combined to feed the EVA tunable resonator. The signal is then attenuated before going into an Agilent 4448A Spectrum Analyzer (SA). The intermodulation powers are read from the output spectrum and recorded for several input power levels and frequency separations. Fig. 20 shows an example measured spectrum with an input power of 5 dBm and Δf of 10 kHz. Whereas the IM3 is clearly visible, the fifth order intermodulation product (IM5) is too low to be observed.

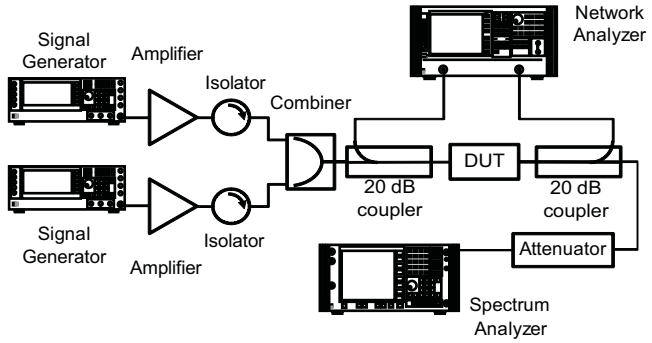

Fig. 19. Measurement setup for two-tone intermodulation characterization.

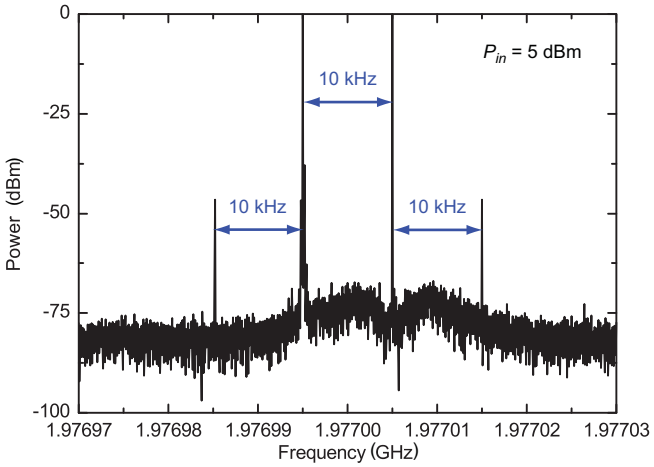

Fig. 20. An example measured output spectrum for the two-tone test of the EVA resonator with $P_{in} = 5$ dBm and $\Delta f = 10$ kHz.

The measured and simulated IM3 values with respect to input power P_{in} $(10 - 25$ dBm) with a frequency separation of 20 kHz are shown in Fig. 21. The extracted IIP3 for the resonator is 58.2 dBm. It is to be noted that the mechanical frequency of the diaphragm tuner is in the kHz range and therefore the deflection of the diaphragm tuner does not respond to the instantaneous change in RF signal power. In other words, the diaphragm responds only to the RF power envelope change in the kHz range. For signals whose envelope change much faster, the tunable filter remains quite linear.

B. MEMS EVA Tunable Filter

A 2% two-pole EVA filter has been designed and fabricated for high power characterization. The design of the filter follows a similar process described in [4]. Since the fractional bandwidth (FBW) of the tested filter is larger than the FBW of the filter in [4], it is expected that the tested filter will exhibit higher power handling capability. The nominal dimensions of the EVA resonators used to design the filter are same as in Section. IV-A. Fig. 22(a) shows an illustration of the designed two-pole filter.

The fabricated tunable filter is shown in Fig. 22(b)(c). The measured linear responses of the tunable filter under several bias voltages are shown in Fig. 22(d). The filter is continuously tunable from 2.35 GHz to 3.21 GHz with less than 110 V bias voltage. The measured insertion loss is $1.65 - 1.42$ dB

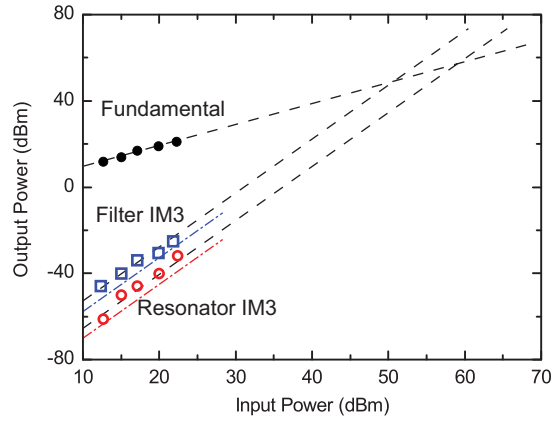

Fig. 21. Measured fundamental output power and IM3 for EVA resonators and filters. The dotted dash lines represent simulation results.

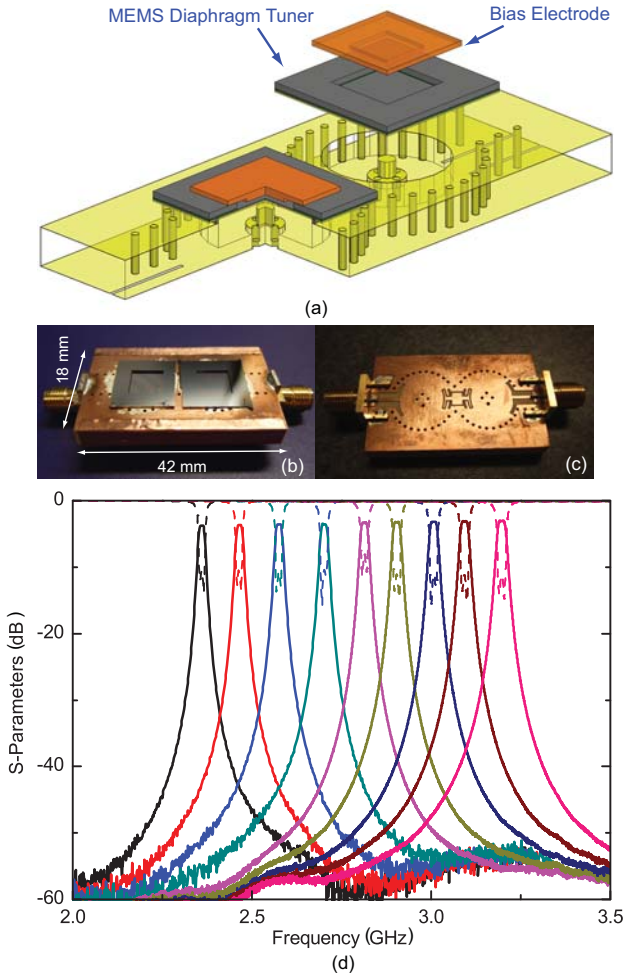

Fig. 22. (a) Illustration of the designed two-pole EVA tunable filter. (b) Fabricated EVA tunable filter. (c) Measured linear responses of the fabricated EVA tunable filter.

(including the loss of the connectors), which translates to an Q_u of $356 - 405$. The extracted initial gaps for the two resonators are 8.2 μm and 9.7 μm respectively. The input and output transformer ratio is extracted to be 8.47 by matching the ADS simulation with small signal measurement.

Fig. 23 shows the measured self-actuation characteristics of the filter at 2.4 GHz. The 3-dB bandwidth of the filter is 47.4

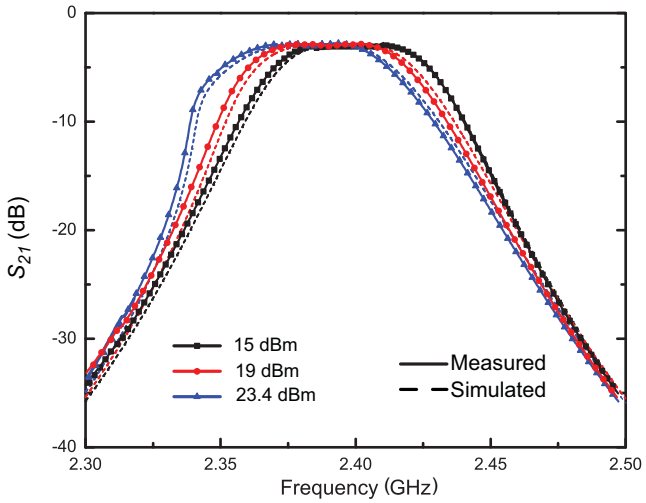

Fig. 23. Measure and simulated large signal S_{21} at 2.4 GHz with several input power levels.

MHz (2%). The required bias voltages on the two resonators are 23.4 V and 36.7 V respectively. For input power less than 15 dBm, there is no significant distortion in the frequency response. As the input power increases beyond 15 dBm, the S_{21} bends towards the lower frequency as predicted by the CAD models in Section. III. The bifurcation instability of one of the resonators occurs at 23.4 dBm. The measured IIP3 of the filter is 52.1 dBm (Fig. 21). There is a very good agreement between the measurement and simulation using the CAD model. These are the worst case results (0 V bias). No attempt to compensate them with higher bias voltages has been made in these measurements.

V. Conclusion

This paper presents a validated complete theoretical framework for estimating the power handling capabilities of EVA RF MEMS tunable resonators and filters. It has been shown that the frequency dependent RF voltage inside a resonator must be taken into account when analyzing the non-linear effects. A practical non-linear circuit model is also employed for analyzing more complex filter structures. The theory and CAD modeling are validated by power measurements on an MEMS EVA tunable resonator and a medium-power two-pole EVA tunable filter. The measured two-pole 2% EVA tunable filter handles 23.4 dBm (0.22 W) RF power before bifurcation instability occurs. The power handling capabilities of the EVA tunable filter can be increased by either increasing the initial gap or the stiffness of the diaphragm actuator at the expense of increased bias voltage or decreased tuning range. Careful consideration of these parameters is necessary to meet the requirements of specific applications.

References

[1] H. Joshi, H. H. Sigmarsson, D. Peroulis, and W. J. Chappell, "Highly Loaded Evanescent Cavities for Widely Tunable High-Q Filters", *2007 IEEE MTT-S Int. Microwave Symp. Dig.*, pp. 2133-2136, Jun. 2007.

[2] X. Liu, L. P. B. Katehi, W. J. Chappell, and D. Peroulis, "A 3.4-6.2 GHz Continuously Tunable Electrostatic MEMS Resonator with Quality Factor of 460-530", *2009 IEEE MTT-S International Microwave Symposium*, Jun. 2009.

[3] S. Park, I. Reines, and G. Rebeiz, "High-Q RF MEMS Tunable Evanescent-mode Cavity Filter," *2009 IEEE MTT-S International Microwave Symposium*, Jun. 2009.

[4] X. Liu, L. P. B. Katehi, W. J. Chappell, and D. Peroulis, "High-Q Tunable Microwave Cavity Resonators and Filters using SOI-based RF MEMS Tuners", *IEEE/ASME Journal of Microelectromechanical System*, vol. 19, no. 4, pp. 774-784, Aug. 2010.

[5] M. Yu, "Power-handling capability for RF filters", *Microwave Magazine*, vol. 8, no. 5, pp 88-97, Oct. 2007.

[6] G. M. Rebeiz, *RF MEMS, Theory, Design and Technology*, New York: J. Wiley & Sons, 2003.

[7] D. Peroulis, L. P. B. Katehi, "Electrostatically-tunable analog RF MEMS varactors with measured capacitance range of 300",*2003 IEEE MTT-S International Microwave Symposium*, vol. 3, pp. 1793-1796, June 2003.

[8] L. Dussopt and G. M. Rebeiz, "Intermodulation distortion and power handling in RF MEMS switches, varactors, and tunable filters," *IEEE Trans. Microw. Theory & Tech.*, vol. 51, no. 4, pp. 927-930, Apr. 2003.

[9] M. Innocent, P. Wambacq, S. Donnay, H. A. C. Tilmans, W. Sansen, and H. DeMan, "An analytic Volterra-series-based model for a MEMS variable capacitor," *IEEE Trans. Comput.-Aided Des. Integr. Circuits Syst.*, vol. 22, no. 2, pp. 124-131, Feb. 2003

[10] D. Girbau, N. Otegi, L. Pradell, A. Lazaro, "Study of intermodulation in RF MEMS variable capacitors," *IEEE Trans. Microwave Theory & Tech.*, vol. 54, no. 3, pp. 1120–1130, Mar. 2006.

[11] D. Peroulis, S. P. Pacheco, L. P. B. Katehi, "RF MEMS switches with enhanced power-handling capabilities," *IEEE Trans. Microw. Theory & Tech.*, vol. 52, no. 1, pp. 59-68, Jan. 2004

[12] R. Gaddi, J. Iannacci, and A. Gnudi, "Mixed-domain simulation of intermodulatio distortion in RF-MEMS capacitive shunt switches," in *33rd Eur. Microw. Conf.*, vol. 2, pp. 671-674, Oct. 2003.

[13] V. Rizzoli, D. Masotti, F. Mastri, and A. Costanzo, "Nonlinear distortion and instability phenomena in MEMS-reconfigurable microstrip antennas," *Proc. 35th Eur. Microw. Conf.*, pp. 565-568, Oct. 2005.

[14] J. Johnson, G. G. Adams, and N. E. McGruer, "Determination of intermodulation distortion in a MEMS microswitch," *IEEE MTT-S Int. Microw. Symp. Dig.*, pp. 2135-2138, Jun. 2005.

[15] X. Liu, L. P. B. Katehi, W. J. Chappell, and D. Peroulis, "Power Handling Capability of High-Q Evanescent-mode RF MEMS Resonators with Flexible Diaphragm", *2009 Asia-Pacific Microwave Conference*, Dec. 2009.

[16] Y. Lu, L. P. B. Katehi, and D. Peroulis, "High-power MEMS varactors and impedance tuners for millimeter-wave applications," *IEEE Trans. Microw. Theory & Tech.*, vol.53, no.11, pp. 3672-3678, Nov. 2005

[17] A. E. Atia and A. E. Williams, "Narrow-Bandpass Waveguide Filters," *IEEE Trans. Microw. Theory & Tech.*, vol.20, no.4, pp. 258-265, Apr. 1972

[18] Y. Lu, "RF MEMS Devices and Their Applications in Reconfigurable RF/Microwave Circuits", *Ph.D Dissertation*, University of Michigan, 2005.

[19] Wolfram Research, Inc., "Mathematica, Version 7.0," Champaign, IL, 2008.

[20] J. A. Pelesko and D. H. Bernstein, *Modeling MEMS and NEMS*,, CRC Press, 2003

[21] Agilent Technologies, "Custom Modeling with Symbolically-Defined Devices," *Advanced Design Systems Documentation.*

[22] B. Atwood, B. Warneke, and K. S. J. Pister, "Preliminary Circuits for Smart Dust," *2000 Southwest Symposium on Mixed-Signal Design*, pp.87-92, 2000

[23] M. R. Hoque, T. McNutt, J. Zhang, A. Mantooth, M. Mojarradi, "A High Voltage Dickson charge pump in SOI CMOS," *Proceedings of the IEEE 2003 Custom Integrated Circuits Conference*, pp. 493-496, Sep. 2003

Xiaoguang Liu (S'07) received the Bachelor's degree in electrical engineering from Zhejiang University, China in 2004 and the Ph.D. degree from Purdue University, USA in 2010. He is currently a postdoctoral research associate with the Department of Electrical and Computer Engineering and Birck Nanotechnology Center, Purdue University. He will be joining the Department of Electrical and Computer Engineering, University of California, Davis, starting from November 1, 2011. Dr. Liu's research interests include novel MEMS/NEMS devices, RF MEMS and high-Q tunable components for reconfigurable radio frontends, microwave, millimeter wave and THz electronics and antennas. Dr. Liu has published more than 20 refereed conference and journal papers. As a student, he was awarded the graduate fellowship from IEEE Antenna and Propagation Society.

Linda P. B. Katehi (S'81-M'84-SM'89-F'95) is currently the Chancellor at the University of California at Davis. She has authored or coauthored over 600 papers published in refereed journals and symposia proceedings, as well as nine book chapters. She holds 13 U.S. patents. Her research is focused on the development and characterization of 3-D integration and packaging of integrated circuits with a particular emphasis on MEMS devices, high-Q evanescent mode filters, and the theoretical and experimental study of planar circuits for hybrid-monolithic and monolithic oscillators, amplifiers, and mixer applications.

Prof. Katehi is a member of the National Academy of Engineering, the Nominations Committee for the National Medal of Technology, the Kauffman National Panel for Entrepreneurship, the National Science Foundation (NSF) Advisory Committee to the Engineering Directorate, and numerous other engineering and scientific committees. She has been the recipient of numerous national and international technical awards and to distinctions as an educator.

William J. Chappell (S'98-M'02) received the B.S.E.E., M.S.E.E., and Ph.D. degrees from The University of Michigan at Ann Arbor, in 1998, 2000, and 2002, respectively.

He is currently an Associate Professor with the Electrical and Computer Engineering Department, Purdue University, West Lafayette, IN, and is also a member of the Birck Nanotechnology Center and the Center for Wireless Systems and Applications. His research focus is on advanced applications of RF and microwave components. He has been involved with numerous Defense Advanced Research Projects Agency (DARPA) projects involved in advanced packaging and materials processing for microwave applications. His research sponsors include Homeland Security Advanced Research Projects Agency (HSARPA), Office of Naval Research (ONR), National Science Foundation (NSF), the State of Indiana, Communications-Electronics Research, Development, and Engineering Center (CERDEC), U.S. Army Research Office (ARO), as well as industry sponsors. His research group uses electromagnetic analysis, unique processing of materials, and advanced design to create novel microwave components. His specific research interests are the application of very high-quality and tunable components utilizing package-scale multilayer components. In addition, he is involved with high-power RF systems, packages, and applications.

Dr. Chappell was the recipient of the URSI Young Scientist Award, the Joel Spira Teaching Excellence Award, and the Eta Kappa Nu 2006 Teacher of the Year Award presented by Purdue University.

Dimitrios Peroulis (S'99-M'04) received his PhD in Electrical Engineering from the University of Michigan at Ann Arbor in 2003. He has been with Purdue University since August 2003 where he is currently leading a group of graduate students on a variety of research projects in the areas of RF MEMS, sensing and power harvesting applications as well as RFID sensors for the health monitoring of sensitive equipment. He has been a PI or a co-PI in numerous projects funded by government agencies and industry in these areas. He is currently a key contributor in two DARPA projects at Purdue focusing on 1) very high quality (Q¿1,000) RF tunable filters in mobile form factors (DARPA Analog Spectral Processing Program, Phases I, II and III) and on 2) developing comprehensive characterization methods and models for understanding the viscoelasticity/creep phenomena in high-power RF MEMS devices (DARPA M/NEMS S&T Fundamentals Program, Phases I and II). Furthermore, he is leading the experimental program on the Center for the Prediction of Reliability, Integrity and Survivability of Microsystems (PRISM) funded by the National Nuclear Security Administration. In addition, he is heading the development of the MEMS technology in a U.S. Navy project (Marines) funded under the Technology Insertion Program for Savings (TIPS) program focused on harsh-environment wireless micro-sensors for the health monitoring of aircraft engines. He has over 110 refereed journal and conference publications in the areas of microwave integrated circuits and antennas. He received the National Science Foundation CAREER award in 2008. His students have received numerous student paper awards and other student research-based scholarships. He has also received eight teaching awards including the 2010 HKN C. Holmes MacDonald Outstanding Teaching Award and the 2010 Charles B. Murphy award, which is Purdue University's highest undergraduate teaching honor.